catalysts

MDPI

Article

The Effects of CeO_2 Nanorods and CeO_2 Nanoflakes on Ni–S Alloys in Hydrogen Evolution Reactions in Alkaline Solutions

Meiqin Zhao [1,2,†], Yao Li [1,2,†], Haifeng Dong [1,2], Lixin Wang [1,2], Zhouhao Chen [1,2], Yazhou Wang [1,2], Zhiping Li [1,2,*], Meirong Xia [1,2,*] and Guangjie Shao [1,2,*]

1 State Key Laboratory of Metastable Materials Science and Technology, Yanshan University, Qinhuangdao 066004, China; zmq_4055@163.com (M.Z.); liyao930421@163.com (Y.L.); hfdong@ysu.edu.cn (H.D.); wanglixin@stumail.ysu.edu.cn (L.W.); chenzh2342@foxmail.com (Z.C.); wangyazhou1121@163.com (Y.W.)

2 Hebei Key Laboratory of Applied Chemistry, College of Environmental and Chemical Engineering, Yanshan University, Qinhuangdao 066004, China

* Correspondence: zpli@ysu.edu.cn (Z.L.); xmr0125@ysu.edu.cn (M.X.); shaoguangjie@ysu.edu.cn (G.S.); Tel.: +86-335-806-1569 (G.S.)

† These authors contributed equally to this study.

Academic Editor: Luísa Margarida Martins

Received: 8 May 2017; Accepted: 16 June 2017; Published: 27 June 2017

Abstract: Composite coatings synthesized by different morphologies of CeO_2 in supergravity devices are highly active in hydrogen evolution reactions (HERs). By adding CeO_2 nanoflakes (CeO_2 Nf) or CeO_2 nanorods (CeO_2 Nr), the change in the microstructures of composites becomes quite distinct. Moreover, most Ni–S alloys are attached on the surface of CeO_2 and roughen it compare with pure CeO_2. In order to make the expression more concise, this paper uses M instead of Ni–S. At a current density of 10 mA/cm^2, overpotentials of Ni–S/CeO_2 Nr (M–CeO_2 Nr) and Ni–S/CeO_2 Nf (M–CeO_2 Nf) are 200 mV and 180 mV respectively, which is lower than that of Ni–S (M-0) coating (240 mV). The exchange current density (j_0) values of M–CeO_2 Nf and M–CeO_2 Nr are 7.48 mA/cm^2 and 7.40 mA/cm^2, respectively, which are higher than that of M-0 (6.39 mA/cm^2). Meanwhile, double-layer capacitances (C_{dl}) values of M–CeO_2 Nf (6.4 mF/cm^2) and M–CeO_2 Nr (6 mF/cm^2) are 21.3 times and 20 times of M-0 (0.3 mF/cm^2), respectively.

Keywords: CeO_2; Ni–S alloy; hydrogen evolution reaction; alkaline solution; morphologies

1. Introduction

It is known to all that populations, food, energies, natural sources, and environmental problems are major threats to the survival and sustainable development of human beings. For the development of industries especially, energy issues urgently need to be resolved. Energies conducive to the development of human beings and the environment have been found and used, such as solar energy, wind energy, and hydrogen energy [1–6]. Moreover, hydrogen energy as a kind of important carbon-free and easily prepared and collected energy has aroused widespread interest [7–11]. For pure metals, the overpotentials of platinum-group metals are the lowest for hydrogen evolution reactions (HERs), but their prices are prohibitively expensive for widespread use [12,13]. In order to reduce the cost, other metals need to be substituted. Thus, these cheaper metals, such as Ni, Fe, and Co, with relatively low overpotentials and in an adequate supply on the planet, are being extensively applied [12]. In addition, their ion states can interact with each other to enhance the catalytic activity of HERs [12–14]. Now, various transition metals (Fe, Co, Ni, Cu, and Mo) have been deemed as

high-efficiency catalysts in HERs [12,14–17]. Additionally, there have been many studies on Ni-based materials, such as Ni–Mo [16], Ni–P [18], Ni–W [13], and Ni–S [19], whose morphologies are different.

The properties of materials are closely related to their morphologies. Many studies about the lamellar structures of materials have been conducted. For instance, Choy et al. synthesized a new lamellar TiO_2-pillared MoS_2 via an extoliation-reassembling method [20]. Lan et al. reported a coupled molybdenum carbide on reduced graphene oxide electrocatalysts for efficient hydrogen evolution [21]. In other studies, materials have presented a rod-like or tubulose structure. Adding a rod-like and tubulose structure substance can also form a material with a new morphology. For example, by electrospinning, Du et al. prepared a new WO_{3-x} catalyst on carbon nanofiber mats, and was found to have a small overpotential with a highly exchanged current density for HERs [22]. Shao et al. reported a new wool-ball-like Ni–carbon nanotube composite, which is favorable for the electrocatalytic activity of HERs [8].

As a rare earth oxide, CeO_2, which has a large number of empty and half-filled d orbitals, unique f orbitals and cheaper market price, is an excellent composite phase that has a synergistic effect with an Ni matrix and is widely studied [23,24]. Therefore, for the CeO_2 system, researchers have concentrated on the morphology and structure of CeO_2. For instance, Li et al. found that CeO_2 nanorods are more reactive in CO oxidation [25]. Wang et al. studied the morphology and crystal-plane effects of CeO_2 on Ru/CeO_2 catalyst in chlorobenzene catalyzed combustion [26]. Li et al. studied the effects of different magnitudes of CeO_2 on Ni–S and Ni–Zn coatings in the catalytic activities of HERs [23,24]. Our team studied the catalytic activities of Ni–CeO_2 and Ni–S/CeO_2 composites in hydrogen evolution [27,28]. In this paper, we prepared different morphologies of CeO_2 and studied the impacts of different CeO_2 morphologies on Ni–S alloys in HERs. First, using the precipitation method, we prepared different morphologies of CeO_2, which were mainly plate-shaped and rod-shaped. However, the precipitants and the reaction temperatures were not the same. Then, formerly prepared CeO_2 was added to solutions to synthesize different coatings. By comparing with the electrochemical performance of Ni–S alloy coatings, it was found that the catalysts supplemented with CeO_2 caused a higher catalytic activity in HERs.

2. Results and Discussion

According to the experiment, we have raised a simple method for the fabrication of Ni–S/CeO_2 (in this paper, Ni–S is presented as "M") composite materials. As shown in Figure 1, the coating is prepared by adding CeO_2 Nr or CeO_2 Nf to the solution containing $Ni(NH_2SO_3)_2{\cdot}4H_2O$, $NiCl_2{\cdot}6H_2O$, NH_4Cl, and thiourea and then by electrodeposition. In the electric fields, part of the nickel ions and sulfur ions formed Ni–S alloys by interaction. However, because of the insufficient use of current efficiency, massive nickel ions and sulfur ions remain in the solution without combination. In our study, an Ni–S alloy was deposited onto a copper substrate in a supergravity device, while some CeO_2 was likely to be the substrate of the Ni–S alloy, embedded in the coating, or attached to the surface of the coating.

Figure 2a displays the XRD of Ni–S/CeO_2 composite materials. In the XRD image of the coating without adding CeO_2, two strong peaks appear at 44.6° and 49.9° that can be ascribed as (202) and (113), which are features of Ni_3S_2 (JCPDS card No. 08-0126). There are wide diffraction peaks at 44° in all plots, so we can say that there are Ni–S alloys in coatings [29,30]. Due to tiny amounts of self-made CeO_2 of the coatings, the diffraction peaks of CeO_2 are very weak. In the XRD patterns of CeO_2 (Figure 2b), three stronger peaks present at 28.6°, 47.5°, and 53.6° are consistent with (111), (220), and (311) planes of standard CeO_2 (JCPDS card No. 04-0593).

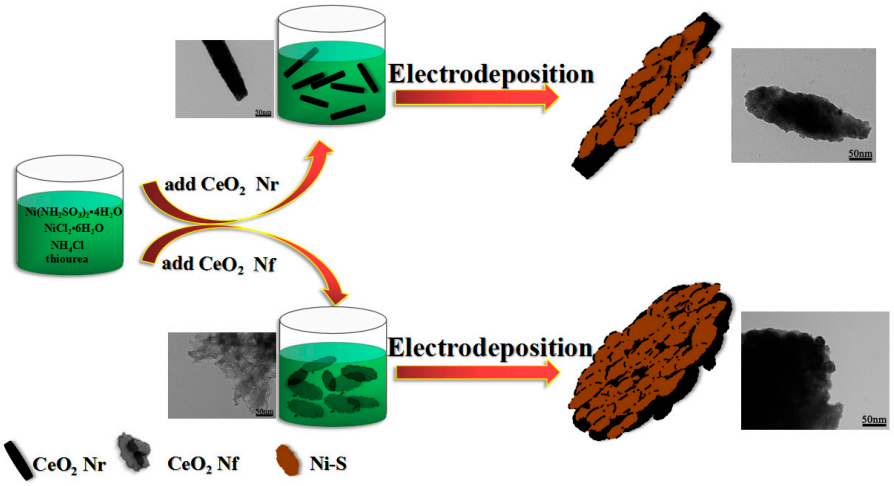

Figure 1. Schematic diagram of Ni–S/CeO_2 synthesis.

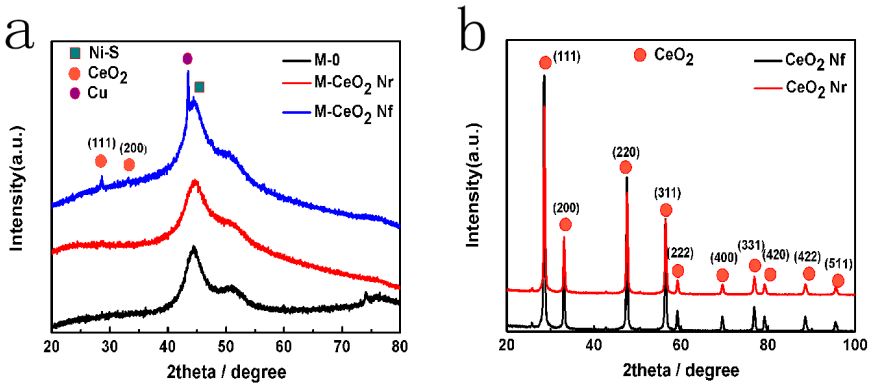

Figure 2. XRD images of (**a**) Ni–S/CeO_2 composite materials and (**b**) CeO_2 nanoflakes and CeO_2 nanorods.

As shown in Figure 3, the morphologies of the composites are different with the addition of CeO_2. Compared with the Ni–S alloy (Figure S1), the particles of Ni–S/CeO_2 (Figure 3A1–B1) become smaller, i.e., their relative specific surface areas are larger after CeO_2 is added. Figure 3A1 is an SEM image of Ni–S/CeO_2 with the addition of CeO_2 nanorods and shows that global particles of different sizes are closely stacked. The TEM image of CeO_2 nanorods in Figure 3A3 show their solid internal structures and their smooth surfaces. However, in the TEM image of the complex (Figure 3A2), the rod shape is irregular, and the rod's surface is rough, perhaps because the Ni–S alloy grew on the exterior of the CeO_2 nanorods. Figure 3B1 shows the rough surface and dense ball-flower resulting from the addition of CeO_2 nanoflakes. Another TEM image of CeO_2 nanoflakes (Figure 3B3) shows a large slice with a definite thickness. Figure 3B2 clearly shows that the presence of particles on the edge and particles adhered to the slice.

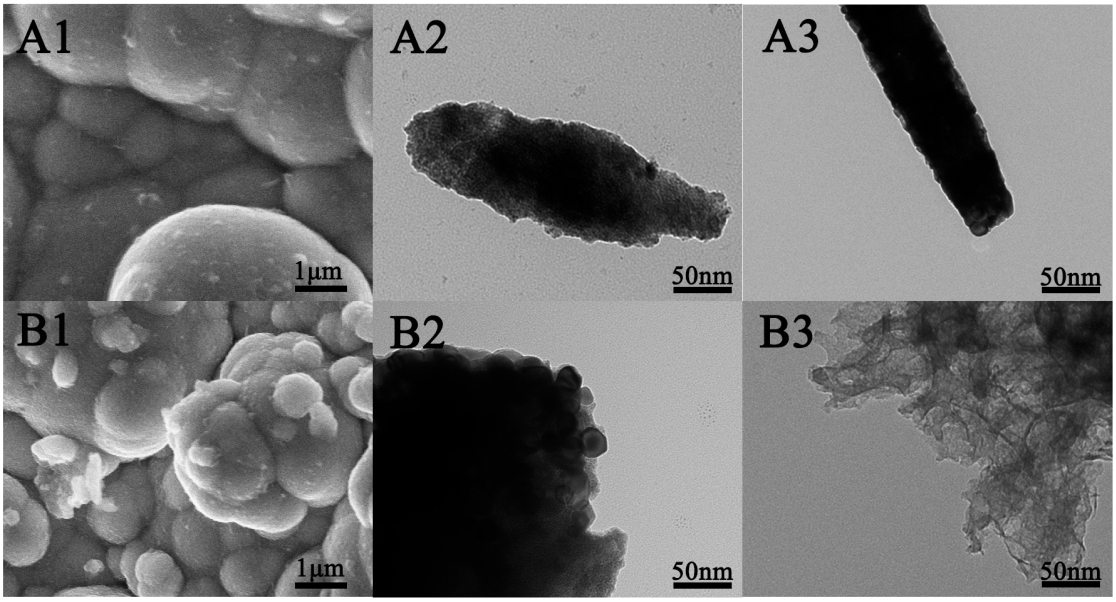

Figure 3. SEM and TEM images of (**A1**,**A2**) M–CeO_2 Nr and (**B1**,**B2**) M–CeO_2 Nf, respectively. TEM images of (**A3**) CeO_2 nanorods and (**B3**) CeO_2 nanoflakes.

IR compensation was performed to correct the polarization data by determining the solution resistance value from the electrochemical impedance spectroscopy measurements. Figure 4a reveals the iR-corrected LSV curve of the three different catalysts. Compared with M-0 (i.e., the Ni–S alloy), the Ni–S/CeO_2 Nf (M–CeO_2 Nf) catalyst displays superior HER activity. As Figure S2 shows, the generation of hydrogen on the electrode surface is dense and intense when the current density is 100 mA/cm^2 [31]. Meanwhile, the overpotentials of M–CeO_2 Nf are lower than those of M-0 and Ni–S/CeO_2 Nr (M–CeO_2 Nr) at the same current density. For instance, at a current density of 10 mA/cm^2, the overpotential of M–CeO_2 Nf coating is 180 mV, which is lower than that of the M–CeO_2 Nr (200 mV) and M-0 (240 mV). Moreover, at a current density of 60 mA/cm^2, the overpotentials of M-0, M–CeO_2 Nr, and M–CeO_2 Nf are 420 mV, 265 mV, and 220 mV, respectively. In order to further study the electrochemical properties, the Tafel plots of the three different samples are detected. As we all know, the Tafel curve matches the Tafel equation ($\eta = a + b\log|j|$), in which b (mV/dec) is the Tafel slope, and j (mA/cm^2) is the current density [22]. According to the values of the Tafel slope (Table 1), it is easy to achieve the fundamental steps in the HER. In the alkaline medium, the reaction steps of catalytic hydrogen evolution are as follows [17,32,33]

$$H_2O + M + e^- \rightarrow MH_{ads} + OH^- \quad \text{(Volmer reaction)}$$

$$MH_{ads} + H_2O + e^- \rightarrow H_2 + M + OH^- \quad \text{(Heyrovsky reaction)}$$

$$MH_{ads} + MH_{ads} \rightarrow H_2 + 2M \quad \text{(Tafel reaction)}$$

That the Tafel slope of M–CeO_2 Nf is 158 mV/dec, which was almost lower than that of M–CeO_2 Nr (163 mV/dec) and M-0 (173.37 mV/dec), indicates that the Volmer reaction is the rate-limiting step in the Volmer-Heyrovsky mechanism. The comparatively low slopes of M–CeO_2 Nf and M–CeO_2 Nr are accompanied by smaller overpotentials at a large current density. Moreover, the addition of CeO_2 to the coating can provide a greater specific surface area to enhance contact with the electrolyte [27,34], which is beneficial to the practical application of the catalyst in the HER. Meanwhile, due to empty and half-filled d orbitals of Ce atoms and oxygen vacancies of CeO_2 [23,24], H_{ads} can easily form on its surfaces. Therefore, there are significant differences in the number of catalytic activity sites for the three samples.

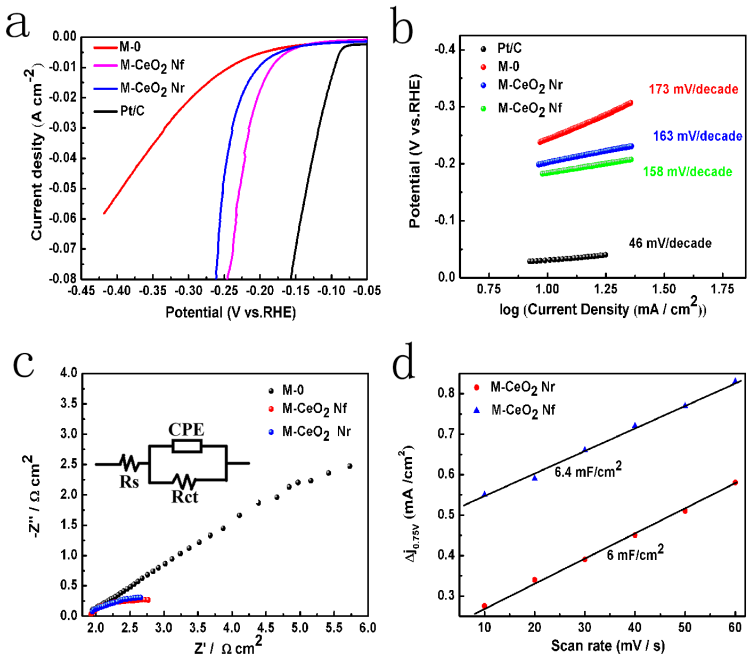

Figure 4. (**a**) Polarization curves obtained for three catalysts. (**b**) Corresponding Tafel plots. (**c**) electrochemical impedance spectra (EIS) of the three catalysts at η = 200 mV. Illustration is an equivalent circuit. (**d**) Liner fitting of the capacitive current of catalysts vs. scan rates. The selected potential range where no faradic was tested is 0.025 V to 0.125 V vs. RHE.

Table 1. Electro-catalytic performances of the three different catalysts.

Paramater	M-0	M–CeO_2 Nr	M–CeO_2 Nf
η_{10} (mV)	240	200	180
Tafel slope (mV dec^{-1})	173	163	158
j_0 (mA cm^{-2})	6.39	7.40	7.48
C_{dl} (mF cm^{-2})	0.3	6	6.4

η_{10} (mV) refers to the overpotential at current density j = 10 mA cm^{-2}.

The exchange current density (j_0) is another test method to prove the activity of the catalyst. As shown in Table 1, j_0 values of M–CeO_2 Nf and M–CeO_2 Nr are 7.48 mA/cm^2 and 7.40 mA/cm^2, respectively, which are higher than that of M-0 (6.39 mA/cm^2). Moreover, the coatings of M–CeO_2 Nf and M–CeO_2 Nr are superior to those of other similar materials, as shown in Table S1. This is attributed to the addition of CeO_2 Nf (or Nr) to add more charge transfer channels to facilitate the formation of H_{ads} [24,35–40]. In order to detect the kinetics of the electrode, electrochemical impedance spectra (EIS) were obtained. Figure 4c shows the Nyquist plots of the three different samples at η = 200 mV. The equivalent circuit is displayed in Figure 4c. For the solution resistance (R_s), all of the values of the electrodes were approximately 2 Ω, but values of the charge transfer resistance (R_{ct}) are quite different, as shown in Table S2. The R_{ct} value of M–CeO_2 Nf is about 2.46 Ω, which is smaller than those of other samples. As we all know, R_{ct} is closely related with hydrogen evolution reaction; that is, the smaller R_{ct} is, the more superior the catalytic activity of the HER is [30–33,41]. Obviously, as discussed above, M–CeO_2 Nf, which holds a smaller R_{ct} and possesses more active sites, shows superior catalytic activity in HERs.

To calculate the effective specific surface area of the catalyst and qualitatively describe the electrochemical activity sites, one impactful way is to reckon the electrochemical double-layer capacitances (C_{dl}) [42–44], which is measured by half the slope of the straight line fitted by the difference between the current density of the anode and the cathode ($\Delta j = j_a - j_c$ at the potential of

0.775 V) at different sweep speeds in the CV curves. To make the CV curve, the selected potential range where there is no faradic is 0.025 V to 0.125 V vs. RHE, and sweep speed range is 10 mV/s to 60 mV/s. C_{dl} values of M–CeO_2 Nf and M–CeO_2 Nr are 6.4 mF/cm^2 and 6 mF/cm^2, which is 21.3 times and 20 times that of M-0 (0.3 mF/cm^2 in Figure S3). respectively. Compared with M-0, M–CeO_2 Nf and M–CeO_2 Nr have larger specific surface areas. This suggests that the two samples with added CeO_2 have more active sites to promote the catalytic activity of the HER, which is consistent with the previous speculation.

The stability of the electrode was measured using CV and CP tools with an electrochemical workstation. CV plots were tested at a scan rate of 100 mV/s between −0.825 V and −1.025 V in a 1 M NaOH solution. CP measurement was carried out at a current density of 100 mA/cm^2 in a 1 M NaOH electrolyte solution. SEM images of M–CeO_2 Nr and M–CeO_2 Nf after 3000 cycles are shown in Figure 5a,c. It can be clearly seen that coatings whose surfaces are rougher than before 3000 cycles are etched in an alkaline solution. However, its overall microstructure is almost unchanged, especially for M–CeO_2 Nf. Similarly, the SEM image of M-0 after 3000 cycles shows also almost no change (Figure S4). Figure 5b shows that the LSV curves of M–CeO_2 Nr before and after 3000 cycles are almost coincident, and the value of the voltage was not alterant in the inset image. Therefore, the stability of M–CeO_2 Nr is superior. The LSV curves of M–CeO_2 Nf are displayed in Figure 5d; like M–CeO_2 Nr, the curves were completely overlaid before and after 3000 cycles, and voltages are unchanged. The stability of M-0 is obtained from Figure S4. It can be concluded that the stabilities of the coatings prepared by electrodeposition are firm, and coatings after a certain period of erosion still did not fall off. With regard to the several samples, the superior catalytic activity in the HER can be attributed to the following points [23,24,45,46]: (i) There is a strong adsorption of hydrogen in the interface of CeO_2 and Ni–S, enhancing the catalytic activity of the HER. (ii) A large amount of the Ni–S alloy is attached to the CeO_2 surface so that more active sites are exposed. (iii) Prepared coatings with added CeO_2 can contact with the electrolyte completely. (iv) There might be a synergistic effect between CeO_2 and Ni–S alloys.

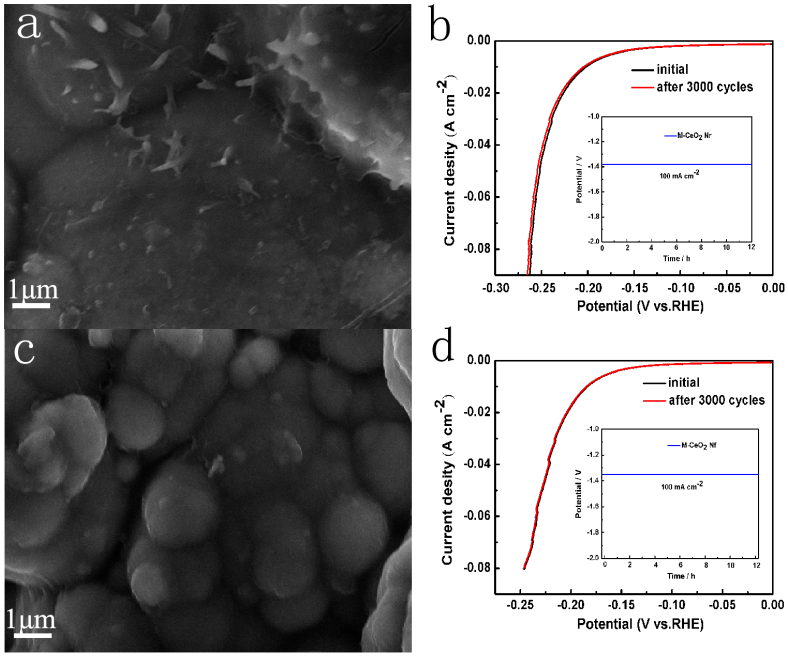

Figure 5. (**a**) SEM of M–CeO_2 Nr after 3000 cycles. (**b**) LSV curves of M–CeO_2 Nr before and after 3000 cycles at a scan rate of 100 mV S^{-1} between −0.825 to −1.025 V. Inset: time dependence of the potential of M–CeO_2 Nr at a current density of 100 mA cm^{-2}. (**c**) SEM of M–CeO_2 Nf after 3000 cycles. (**d**) LSV curves of M–CeO_2 Nf before and after 3000 cycles at a scan rate of 100 mV S^{-1} between −0.825 to −1.025 V. Inset: time dependence of the potential of M–CeO_2 Nf at a current density of 100 mA m^{-2}.

3. Materials and Methods

3.1. Preparation of CeO_2 Nanoflakes and CeO_2 Nanorods

CeO_2 nanoflakes were prepared via the precipitation method. Cerous nitrates (6 g) (Tianjin Kermel Chemical Reagent Co., Tianjin, China) were dissolved in 200 mL of distilled water under magnetic stirring until cerous nitrates completely disappeared. Then, the solution underwent an aging process with the help of a mixed solute of NaOH (Tianjin Kermel Chemical Reagent Co., Tianjin, China) and Na_2CO_3 (Tianjin Kermel Chemical Reagent Co., Tianjin, China) ($NaOH/Na_2CO_3$ = 1:1, n/n), which was acutely stirred for 4 h in an alkaline condition. After suction filtration, the collection was dried at 80 °C all day and heated to 600 °C for 4 h to obtain a powder. CeO_2 nanorods were also made via a precipitation method. A mixed solute of $Ce(NO_3)_3{\cdot}6H_2O$ and $(NH_2)_2CO$ ($Ce(NO_3)_3{\cdot}6H_2O/(NH_2)_2CO$ = 1:40, m/m) was melted in distilled water and then agitated at 90 °C for 4 h. The collection was dried at 80 °C for 48 h and warmed up to 700 °C for 3 h.

3.2. Fabrication of Ni–S/CeO_2

In this paper, complex substances were prepared by one step in supergravity equipment [8,9,46]. A portion of CeO_2 was added into 700 mL of plating solution of 350 g/L $Ni(NH_2SO_3)_2{\cdot}4H_2O$ (Tianjin Kermel Chemical Reagent Co., Tianjin, China), 10 g/L $NiCl_2{\cdot}6H_2O$ (Tianjin Kermel Chemical Reagent Co., Tianjin, China), 30 g/L NH_4Cl (Tianjin Kermel Chemical Reagent Co., Tianjin, China), and 50 g/L thiourea (Tianjin Kermel Chemical Reagent Co., Tianjin, China). Then, the dispersed suspension was treated in a sonic bath for about 1 h. A pure nickel tube was used as the anode, and copper foil was used as the cathode. The pretreatment process consisted of mechanical polishing, followed by the use of ethanol, sodium hydroxide, and dilute hydrochloric acid, successively, in an ultrasonic device for 15 min. Copper foil were then washed with distilled water and dried every time. With the help of a DC-regulated power supply, experiments were carried out at a temperature of 45 °C for 1 h. The Ni–S alloy was synthesized by similar procedures.

3.3. Characterizations

The samples were characterized by SEM (FE-SEM, Carl Zeiss Super55 operated at 20 kV), X-ray power diffraction (RigakuSmart Lab, X-ray Diffractometer, Tokyo, Japan), and TEM (Hitachi HT 7700, transmission electronic microscope, Tokyo, Japan). The chemical compositional analysis was actualized by an energy dispersive spectrometer (EDS), which was attached to the TEM.

3.4. Electrochemical Measurements

All electrochemical measurements were performed with an electrode system in a 1.0 M NaOH on a CHI660E electrochemical workstation. An Hg/HgO electrode (0.097 V vs. standard hydrogen electrode) and a platinum foil were used as a reference electrode and counter electrode, respectively. The composite platings were cut into pieces of 1×1 cm^2, and their backs were bonded with epoxy resin to be used directly as the working electrode. Linear sweep voltammetry (LSV) measurements were carried out at a scan rate of 5 mV s^{-1}, and cyclic voltammetry (CV) measurements were implemented between −0.825 V and −1.025 V at a scan rate of 100 mV s^{-1}. The long-term electrolysis was tested by chronopotentiometry (CP) measurement (V–t). This process was performed at a constant current density of 100 mA cm^{-2} in 1 M NaOH for 12 h. A.C. Impedance measurements were obtained at an overpotential of 200 mV with a wide frequency range from 0.01 Hz to 10 KHz. For all potentials and overpotentials, iR correction was performed.

4. Conclusions

Composite coatings were prepared by a supergravity device by adding different morphologies of CeO_2. Although the uniformity of the two kinds of coating microstructures is poor, the Ni–S alloy

adheres to the surface of CeO_2, and its catalytic activity in HERs is substantial. The overpotentials of M–CeO_2 Nr and M–CeO_2 Nf are 200 mV and 180 mV, respectively. Moreover, the values of the Tafel slope suggest that the Volmer reaction is the rate-limiting step in the Volmer–Heyrovsky mechanism. The exchange current density (j_0) values of M–CeO_2 Nf and M–CeO_2 Nr are 7.48 mA/cm^2 and 7.40 mA/cm^2, respectively, which are higher than that of M-0 (6.39 mA/cm^2). Meanwhile, double-layer capacitances (C_{dl}) values of M–CeO_2 Nf (6.4 mF/cm^2) and M–CeO_2 Nr (6 mF/cm^2) are 21.3 times and 20 times that of M-0 (0.3 mF/cm^2), respectively.

Supplementary Materials: The following are available online at www.mdpi.com/2073-4344/7/7/197/s1, Video S1, Hydrogen evolution with the M-CeO_2(Nr); Figure S1, SEM image of M-0, Figure S2, Image showing hydrogen evolution with the M-CeO_2(Nr), Figure S3, Liner fitting of the capacitive current of M-0 vs. scan rates. The selected potential range where no faradic current was tested is 0.025 V to 0.125 V vs. RHE, Figure S4, (a) SEM of M-0 after 3000 cycles; (b) LSV curves of M-0 before and after 3000 CV cycles at a scan rate of 100 mV S^{-1} between −0.825 to −1.025 V. Inset, time dependence of the potential of M-0 at a current density of 100 mA cm^{-2}, Table S1, Comparison of HER performance in alkaline media for Ni-S/CeO_2(Nr) and Ni-S/CeO_2(Nf) with other non-noble-metal HER electrocatalysts, Table S2, Values of the charge transfer resistance and the mass transfer resistance of four different electrodes.

Acknowledgments: This work was financially supported by the National Natural Science Foundation of China (NO.51674221).

Author Contributions: G.S., H.D., Z.L., and M.X. conceived and designed the experiments; M.Z. and Y.L. performed the experiments, analyzed the data, and wrote the paper. Y.W., L.W., and Z.C. participated in writing the paper.

Conflicts of Interest: The authors declare no conflict of interest.

References

1. Winsche, W.E.; Hoffman, K.C.; Salzano, F.J. Hydrogen: Its future role in the nation's energy economy. *Science* **1973**, *180*, 1325–1332. [CrossRef] [PubMed]
2. Paseka, I. Influence of hydrogen absorption in amorphous Ni–P electrodes on double layer capacitance and charge transfer coefficient of hydrogen evolution reaction. *Electrochim. Acta* **1999**, *44*, 4551–4558. [CrossRef]
3. Liu, W.; Hu, E.; Jiang, H.; Xiang, Y.; Weng, Z.; Li, M.; Fan, Q.; Yu, X.; Altman, E.I.; Wang, H. A highly active and stable hydrogen evolution catalyst based on pyrite-structured cobalt phosphosulfide. *Nat. Commun.* **2016**, *7*, 10771. [CrossRef]
4. Xing, R.; Jiao, T.; Liu, Y.; Ma, K.; Zou, Q.; Ma, G.; Yan, X. Co-assembly of graphene oxide and albumin/photosensitizer nanohybrids towards enhanced photodynamic therapy. *Polymers* **2016**, *8*, 181. [CrossRef]
5. Yang, W.; Yang, W.; Ding, F.; Sang, L.; Ma, Z.; Shao, G. Template-free synthesis of ultrathin porous carbon shell with excellent conductivity for high-rate supercapacitors. *Carbon* **2017**, *111*, 419–427. [CrossRef]
6. Yang, W.; Yang, W.; Song, A.; Gao, L.; Sun, G.; Shao, G. Pyrrole as a promising electrolyte additive to trap polysulfides for lithium-sulfur batteries. *J. Power Sources* **2017**, *348*, 175–182. [CrossRef]
7. Chen, Z.; Ma, Z.; Song, J.; Wang, L.; Shao, G. Novel one-step synthesis of wool-ball-like Ni–carbon nanotubes composite cathodes with favorable electrocatalytic activity for hydrogen evolution reaction in alkaline solution. *J. Power Sources* **2016**, *324*, 86–96. [CrossRef]
8. Wang, L.; Li, Y.; Xia, M.; Li, Z.; Chen, Z.; Ma, Z.; Qin, X.; Shao, G. Ni nanoparticles supported on graphene layers: An excellent 3d electrode for hydrogen evolution reaction in alkaline solution. *J. Power Sources* **2017**, *347*, 220–228. [CrossRef]
9. Ouyang, C.; Wang, X.; Wang, C.; Zhang, X.; Wu, J.; Ma, Z.; Dou, S.; Wang, S. Hierarchically porous Ni_3S_2 nanorod array foam as highly efficient electrocatalyst for hydrogen evolution reaction and oxygen evolution reaction. *Electrochim. Acta* **2015**, *174*, 297–301. [CrossRef]
10. Zhang, R.; Xing, R.; Jiao, T.F.; Ma, K.; Chen, C.; Ma, G.; Yan, X. Carrier-free, chemo-photodynamic dual nanodrugs via self-assembly for synergistic antitumor therapy. *ACS Appl. Mater. Interfaces* **2016**, *8*, 13262. [CrossRef]

11. Song, A.; Yang, W.; Yang, W.; Sun, G.; Yin, X.; Gao, L.; Wang, Y.; Qin, X.; Shao, G. Facile synthesis of cobalt nanoparticles entirely encapsulated in slim nitrogen-doped carbon nanotubes as oxygen reduction catalyst. *ACS Sustain. Chem. Eng.* **2017**, *5*, 3973–3981. [CrossRef]
12. Xiao, P.; Sk, M.A.; Thia, L.; Ge, X.; Lim, R.J.; Wang, J.Y.; Lim, K.H.; Wang, X. Molybdenum phosphide as an efficient electrocatalyst for the hydrogen evolution reaction. *Energy Environ. Sci.* **2014**, *7*, 2624–2629. [CrossRef]
13. Hong, S.H.; Sang, H.A.; Choi, J.; Jin, Y.K.; Kim, H.Y.; Kim, H.J.; Jang, J.H.; Kim, H.; Kim, S.K. High-activity electrodeposited NiW catalysts for hydrogen evolution in alkaline water electrolysis. *Appl. Sur. Sci.* **2015**, *349*, 629–635. [CrossRef]
14. Wang, D.Y.; Gong, M.; Chou, H.L.; Pan, C.J.; Chen, H.A.; Wu, Y.; Lin, M.C.; Guan, M.; Yang, J.; Chen, C.W. Highly active and stable hybrid catalyst of cobalt-doped FeS_2 nanosheets-carbon nanotubes for hydrogen evolution reaction. *J. Am. Chem. Soc.* **2016**, *137*, 1587–1592. [CrossRef] [PubMed]
15. Gao, M.R.; Liang, J.X.; Zheng, Y.R.; Xu, Y.F.; Jiang, J.; Gao, Q.; Li, J.; Yu, S.H. An efficient molybdenum disulfide/cobalt diselenide hybrid catalyst for electrochemical hydrogen generation. *Nat. Commun.* **2015**, *6*, 5982. [CrossRef] [PubMed]
16. Mckone, J.R.; Sadtler, B.F.; Werlang, C.A.; Lewis, N.S.; Gray, H.B. Ni–Mo nanopowders for efficient electrochemical hydrogen evolution. *ACS Catal.* **2013**, *3*, 166. [CrossRef]
17. Bates, M.K.; Jia, Q.; Ramaswamy, N.; Allen, R.J.; Mukerjee, S. Composite Ni/NiO Cr_2O_3 catalyst for alkaline hydrogen evolution reaction. *J. Phys. Chem. C* **2016**, *119*, 5467–5477. [CrossRef] [PubMed]
18. Azarniya, A.; Salatin, F.; Eskandaripoor, M.R.; Rasooli, A. A kinetic study on the mechanism of hydrogen evolution in Ni–P coated titanium hydride powder. *Adv. Powder Technol.* **2015**, *26*, 259–266. [CrossRef]
19. Tang, C.; Pu, Z.; Liu, Q.; Asiri, A.M.; Luo, Y.; Sun, X. Ni_3S_2 nanosheets array supported on Ni foam: A novel efficient three-dimensional hydrogen-evolving electrocatalyst in both neutral and basic solutions. *Int. J. Hydrogen Energy* **2015**, *40*, 4727–4732. [CrossRef]
20. Paek, S.M.; Jung, H.; Park, M.; Lee, J.K.; Choy, J.H. An inorganic nanohybrid with high specific surface area: TiO_2-pillared MoS_2. *Chem. Mater.* **2005**, *17*, 3492–3498. [CrossRef]
21. Li, J.S.; Yu, W.; Liu, C.H.; Li, S.L.; Wang, Y.G.; Dong, L.Z.; Dai, Z.H.; Li, Y.F.; Lan, Y.Q. Coupled molybdenum carbide and reduced graphene oxide electrocatalysts for efficient hydrogen evolution. *Nat. Commun.* **2016**, *7*, 11204. [CrossRef]
22. Chen, J.; Yu, D.; Liao, W.; Zheng, M.; Xiao, L.; Zhu, H.; Zhang, M.; Du, M.; Yao, J. Wo_{3-x} nanoplates grown on carbon nanofibers for an efficient electrocatalytic hydrogen evolution reaction. *ACS Appl. Mater. Interfaces* **2016**, *8*, 18132. [CrossRef] [PubMed]
23. Zheng, Z.; Li, N.; Wang, C.Q.; Li, D.Y.; Meng, F.Y.; Zhu, Y.M.; Li, Q.; Wu, G. Electrochemical synthesis of Ni–S/CeO_2 composite electrodes for hydrogen evolution reaction. *J. Power Sources* **2013**, *230*, 10–14. [CrossRef]
24. Zheng, Z.; Li, N.; Wang, C.Q.; Li, D.Y.; Meng, F.Y.; Zhu, Y.M. Effects of CeO_2 on the microstructure and hydrogen evolution property of Ni–Zn coatings. *J. Power Sources* **2013**, *222*, 88–91. [CrossRef]
25. Zhou, K.; Xu, R.; Sun, X.; Chen, H.; Tian, Q.; Shen, D.; Li, Y. Favorable synergetic effects between CuO and the reactive planes of ceria nanorods. *Catal. Lett.* **2005**, *101*, 169–173. [CrossRef]
26. Huang, H.; Dai, Q.; Wang, X. Morphology effect of Ru/CeO_2 catalysts for the catalytic combustion of chlorobenzene. *Appl. Catal. B* **2014**, *158–159*, 96–105. [CrossRef]
27. Chen, Z.; Ma, Z.; Song, J.; Wang, L.; Shao, G. A novel approach for the preparation of Ni–CeO_2 composite cathodes with enhanced electrocatalytic activity. *RSC Adv.* **2016**, *6*, 60806–60814. [CrossRef]
28. Zhao, M.; Dong, H.; Chen, Z.; Ma, Z.; Wang, L.; Wang, G.; Yang, W.; Shao, G. Study of Ni–S/CeO_2 composite material for hydrogen evolution reaction in alkaline solution. *Int. J. Hydrogen Energy* **2016**, *41*, 20485–20493. [CrossRef]
29. Han, Q.; Li, X.; Chen, J.; Liu, K.; Dong, X.; Wei, X. Study of amorphous Ni–S(La) alloy used as her cathode in alkaline medium. *J. Alloys Compd.* **2005**, *400*, 265–269. [CrossRef]
30. Cao, Y.; Liu, J.; Wang, F.; Ji, J.; Wang, J.; Qin, S.; Zhang, L. Electrodeposited Ni–S intermetallic compound film electrodes for hydrogen evolution reaction in alkaline solutions. *Mater. Lett.* **2010**, *64*, 261–263. [CrossRef]
31. Mali, M.G.; Yoon, H.; Joshi, B.N.; Park, H.; Aldeyab, S.S.; Dong, C.L.; Ahn, S.J.; Nervi, C.; Yoon, S.S. Enhanced photoelectrochemical solar water splitting using a platinum-decorated CIGS/CdS/ZnO photocathode. *ACS Appl. Mater. Interfaces* **2015**, *7*, 21619–21625. [CrossRef] [PubMed]

32. Navarro-Flores, E.; Chong, Z.; Omanovic, S. Characterization of Ni, NiMo, NiW and NiFe electroactive coatings as electrocatalysts for hydrogen evolution in an acidic medium. *J. Mol. Catal. A* **2005**, *226*, 179–197. [CrossRef]
33. González-Buch, C.; Herraiz-Cardona, I.; Ortega, E.; García-Antón, J.; Pérez-Herranz, V. Synthesis and characterization of macroporous Ni, Co and Ni–Co electrocatalytic deposits for hydrogen evolution reaction in alkaline media. *Int. J. Hydrogen Energy* **2013**, *38*, 10157–10169. [CrossRef]
34. Ay, H.; Üner, D. Dry reforming of methane over CeO_2 supported Ni, Co and Ni–Co catalysts. *Appl. Catal. B* **2015**, *179*, 128–138. [CrossRef]
35. Burbano, M.; Norberg, S.T.; Hull, S.; Eriksson, S.G.; Marrocchelli, D.; Madden, P.A.; Watson, G.W. Oxygen vacancy ordering and the conductivity maximum in Y_2O_3-doped CeO_2. *Chem. Mater.* **2012**, *24*, 222–229. [CrossRef]
36. López, J.M.; Gilbank, A.L.; García, T.; Solsona, B.; Agouram, S.; Torrente-Murciano, L. The prevalence of surface oxygen vacancies over the mobility of bulk oxygen in nanostructured ceria for the total toluene oxidation. *Appl. Catal. B Environ.* **2015**, *174–175*, 403–412. [CrossRef]
37. Tan, J.P.Y.; Tan, H.R.; Boothroyd, C.; Yong, L.F.; He, C.B.; Lin, M. Three-dimensional structure of CeO_2 nanocrystals. *J. Phys. Chem. C* **2014**, *115*, 3544–3551. [CrossRef]
38. Bhosale, A.K.; Shinde, P.S.; Tarwal, N.L.; Kadam, P.M.; Mali, S.S.; Patil, P.S. Synthesis and characterization of spray pyrolyzed nanocrystalline CeO_2–SiO_2 thin films as passive counter electrodes. *Sol. Energy Mater. Sol. Cells* **2010**, *94*, 781–787. [CrossRef]
39. Yi, G.; Yuan, Y. Morphology effects of nanocrystalline CeO_2 on the preferential co oxidation in H_2-rich gas over Au/CeO_2 catalyst. *Chem. Phys. Lett.* **2009**, *479*, 128–132. [CrossRef]
40. Wu, Z.; Li, M.; Mullins, D.R.; Overbury, S.H. Probing the surface sites of CeO_2 nanocrystals with well-defined surface planes via methanol adsorption and desorption. *ACS Catal.* **2012**, *2*, 2224–2234. [CrossRef]
41. Liao, L.; Zhu, J.; Bian, X.; Zhu, L.; Scanlon, M.D.; Girault, H.H.; Liu, B. MoS_2 formed on mesoporous graphene as a highly active catalyst for hydrogen evolution. *Adv. Funct. Mater.* **2013**, *23*, 5326–5333. [CrossRef]
42. Zhou, H.; Wang, Y.; He, R.; Yu, F.; Sun, J.; Wang, F.; Lan, Y.; Ren, Z.; Chen, S. One-step synthesis of self-supported porous $NiSe_2$/Ni hybrid foam: An efficient 3d electrode for hydrogen evolution reaction. *Nano Energy* **2016**, *20*, 29–36. [CrossRef]
43. Xie, J.; Zhang, H.; Li, S.; Wang, R.; Sun, X.; Zhou, M.; Zhou, J.; Lou, X.W.; Xie, Y. Defect-rich MoS_2 ultrathin nanosheets with additional active edge sites for enhanced electrocatalytic hydrogen evolution. *Adv. Mater.* **2013**, *25*, 5807–5813. [CrossRef] [PubMed]
44. Xu, K.; Wang, F.; Wang, Z.; Zhan, X.; Wang, Q.; Cheng, Z.; Safdar, M.; He, J. Component-controllable $WS_{(2(1-x))}Se_{(2x)}$ nanotubes for efficient hydrogen evolution reaction. *ACS Nano* **2014**, *8*, 8468–8476. [CrossRef] [PubMed]
45. Tiwari, R.; Sarkar, B.; Tiwari, R.; Pendem, C.; Sasaki, T.; Saran, S.; Bal, R. Pt nanoparticles with tuneable size supported on nanocrystalline ceria for the low temperature water-gas-shift (WGS) reaction. *J. Mol. Catal. A* **2014**, *395*, 117–123. [CrossRef]
46. Du, J.; Shao, G.; Qin, X.; Wang, G.; Zhang, Y.; Ma, Z. High specific surface area MnO_2 electrodeposited under supergravity field for supercapacitors and its electrochemical properties. *Mater. Lett.* **2012**, *84*, 13–15. [CrossRef]